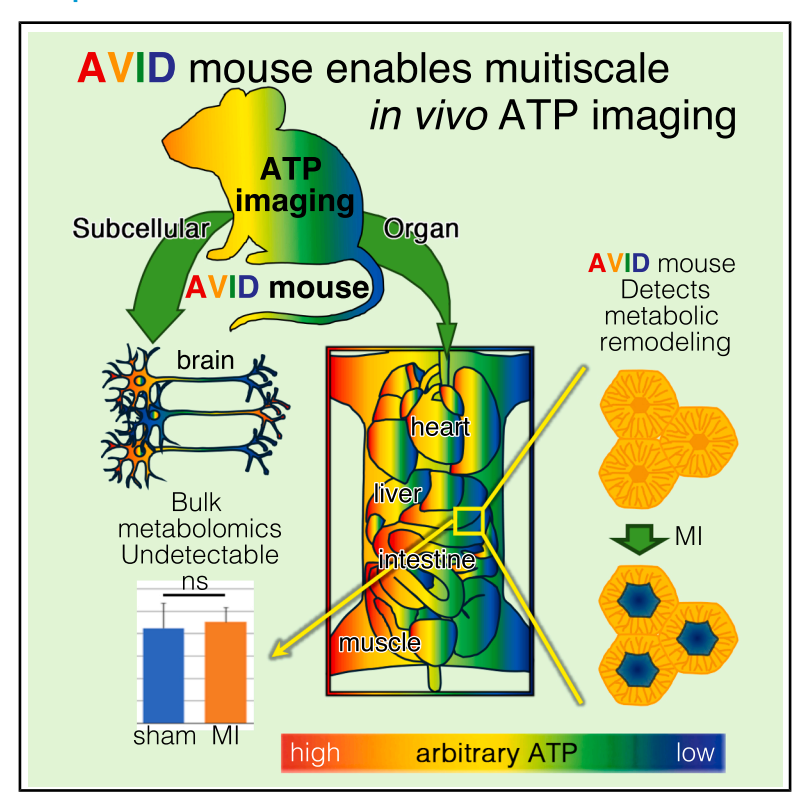
AVID mouse: A versatile platform for real-time, multiscale ATP imaging and spatial systems metabolism analysis in living mice

Graphical abstract



Authors

Yuichiro Ohnishi, Daiki Setoyama, Hideki Miwa, ..., Motoko Yanagita, Hiromi Imamura, Masamichi Yamamoto

Correspondence

myamamoto@ncvc.go.jp

In brief

Ohnishi et al. present the AVID mouse, which enables real-time, multiscale imaging of ATP dynamics in vivo across organs and cell types. This platform reveals spatially heterogeneous changes in energy metabolism during both physiological conditions and pathological states such as myocardial infarction, enabling systems-level analysis of metabolic regulation.

Highlights

- The AVID mouse enables real-time, multiscale ATP imaging in living mice
- Quantitative ATP dynamics were captured across organs and cellular compartments
- Organ-specific responses to physiological and pathological stimuli were visualized
- AVID provides a versatile platform to study spatially resolved energy metabolism in vivo







Resource

AVID mouse: A versatile platform for real-time, multiscale ATP imaging and spatial systems metabolism analysis in living mice

Yuichiro Ohnishi,^{1,22} Daiki Setoyama,^{2,22} Hideki Miwa,^{4,22} Norimichi Koitabashi,⁵ Riki Ogasawara,⁸ Seri Kitada,¹ Naoki Matoba,¹ Takahito Ayano,¹ Kaoru Hiramoto,^{9,10} Ryuto Yasui,¹ Yuki Sugiura,¹¹ Takahisa Anada,^{14,15} Kosuke Ino,¹⁶ Hinako Matsuda,¹ Takahiro Noma,¹ Shigenori Nonaka,^{17,18} Takashi Izumi,⁶ Masahiko Kurabayashi,⁵ Makoto Suematsu,¹⁹ Yuya Kunisaki,³ Motoko Yanagita,^{12,20} Hiromi Imamura,^{13,21} and Masamichi Yamamoto^{1,7,20,23,*}

SUMMARY

We developed the AVID (ATP visualization *in vivo* directly) mouse, a genetically encoded biosensor mouse enabling real-time, multiscale imaging of ATP dynamics across the whole body, organs, and cellular compartments in living animals. AVID revealed previously undetectable localized ATP depletion near the central vein of the liver after myocardial infarction, spatially linked to kynurenic acid accumulation—a phenomenon invisible to conventional bulk metabolomics. By seamlessly integrating macroscopic organ-level imaging with microscopic spatial metabolomics, AVID establishes a new framework for spatial systems metabolism. Beyond myocardial infarction, this platform offers broad applicability to study organ-organ metabolic communication, spatial metabolic heterogeneity, and localized metabolic shifts across diverse physiological and pathological contexts, providing a transformative resource for metabolic research.



¹Department of Research Promotion and Management, National Cerebral and Cardiovascular Center, Kishibe-Shimmachi, Suita, Osaka 564-8565, Japan

²Department of Clinical Chemistry and Laboratory Medicine, Kyushu University Hospital, Fukuoka, Japan

³Department of Clinical Chemistry and Laboratory Medicine, Graduate School of Medical Sciences, Kyushu University, Fukuoka 812-8582, Japan

⁴Department of Neuropsychopharmacology, National Center of Neurology and Psychiatry, Kodaira, Tokyo 187-8553, Japan

⁵Department of Cardiovascular Medicine, Gunma University Graduate School of Medicine, Maebashi, Gunma 371-8511, Japan

⁶Department of Biochemistry, Gunma University Graduate School of Medicine, Maebashi, Gunma 371-8511, Japan

⁷Advanced Scientific Research Leaders Development Unit, Gunma University Graduate School of Medicine, Maebashi, Gunma 371-8511, Japan

⁸Department of Life Science and Applied Chemistry, Nagoya Institute of Technology, Gokiso-cho, Showa-ku, Nagoya, Aichi 466-8555, Japan

⁹Frontier Research Institute for Interdisciplinary Sciences, Tohoku University, Sendai 980-8578, Japan

¹⁰Research Institute of Electrical Communication, Tohoku University, Sendai 980-8577, Japan

¹¹Multiomics Platform, Center for Cancer Immunotherapy and Immunobiology (CCII), Kyoto University, Kyoto 606-8501, Japan

¹²Institute for the Advanced Study of Human Biology (ASHBi), Kyoto University, Kyoto 606-8501, Japan

¹³Department of Functional Biology, Graduate School of Biostudies, Kyoto University, Kyoto 606-8501, Japan

¹⁴Institute for Materials Chemistry and Engineering, Kyushu University, Fukuoka 819-0395, Japan

¹⁵Department of Applied Chemistry, Graduate School of Engineering, Kyushu University, Fukuoka 819-0395, Japan

¹⁶Graduate School of Engineering, Tohoku University, Sendai 980-8579, Japan

¹⁷Spatiotemporal Regulations Group, Exploratory Research Center for Life and Living Systems (ExCELLS), Nishigonaka 38, Myodaiji, Okazaki Aichi 444-8585, Japan

¹⁸Laboratory for Spatiotemporal Regulations, National Institute for Basic Biology (NIBB), Nishigonaka 38, Myodaiji, Okazaki Aichi 444-8585, Japan

¹⁹Central Institute for Experimental Medicine and Life Science and WPI Bio2Q Research Center, Keio University, Kawasaki-city, Kanagawa 210-0821, Japan

²⁰Department of Nephrology, Kyoto University Graduate School of Medicine, Kyoto University, Shogoin-Kawahara-cho, Sakyo-ku, Kyoto 606-8507, Japan

²¹Science Research Center, Organization for Research Initiatives, Yamaguchi University, 1677-1 Yoshida, Yamaguchi 753-8515, Japan ²²These authors contributed equally

²³Lead contact

^{*}Correspondence: myamamoto@ncvc.go.jp https://doi.org/10.1016/j.celrep.2025.116246



Cell ReportsResource

INTRODUCTION

Adenosine triphosphate (ATP) is a crucial energy carrier that drives diverse metabolic and biochemical reactions in all living organisms. 1-4 Given ATP's fundamental role in cellular functions, developing tools to measure ATP dynamics in real time in vivo is essential to advance our understanding of the physiological and pathological mechanisms underlying various biological processes. In vivo imaging of metabolic dynamics at multiple spatial scales-from the whole body to single cells-is essential for understanding spatial systems metabolism, which governs organ-organ metabolic communication and localized metabolic remodeling during disease progression. However, existing tools lack the required spatial and temporal resolution. ATP levels in live cells or tissues can be monitored using genetically encoded biosensors, 5,6 and numerous ATP sensors have been developed with diverse dynamic ranges, subcellular targeting capabilities, and responsiveness to metabolic fluctuations. 7-11 The GO-ATeam 12 is functionally robust in vivo and capable of imaging ATP levels with minimized artifacts by providing a ratio metric readout of Förster resonance energy transfer (FRET). The GO-ATeam was used to monitor ATP in mouse neurons¹³ and zebrafish cardiomyocytes.¹⁴ However, existing techniques such as ATP bioluminescence imaging or FRET-based ATP indicators in isolated cells lack the spatial and temporal resolution required to capture rapid ATP fluctuations in living organisms. Furthermore, traditional methods are often invasive, require tissue extraction, or suffer from low sensitivity in deep tissues. To overcome these limitations, we developed AVID (ATP visualization in vivo directly), a genetically encoded ATP biosensor mouse model that provides a multiscale imaging platform for spatial systems metabolism, allowing real-time, high-resolution ATP imaging from the whole body to individual cells in living animals. This tool provides a unique opportunity to study energy metabolism in both physiological and pathological conditions.

RESULTS

Generation and validation of the AVID mouse for *in vivo* **ATP** imaging

To address this limitation for in vivo ATP imaging, we developed a mouse model in which GO-ATeam expression is controlled by a ubiquitous promoter. Since GO-ATeam requires intramolecular ATP trapping to emit signals, its high-level expression may cause detrimental effects, as observed with the overexpression of the Ca²⁺ sensor GCaMP¹⁵⁻¹⁷ (Figure S1A). To ensure appropriate GO-ATeam expression levels, we employed multiple expression modalities and generated a panel of mouse embryonic stem (ES) cell lines expressing GO-ATeam at varying levels (Figures S1B and 2). Most mouse lines derived from these ES cells exhibited abnormal development or failed to produce offspring. However, one knockin mouse line, termed AVID (Figure S1C), was fertile and produced normal offspring with metabolic profiles and energy expenditure comparable to wild-type (WT) mice (Figures S3A-S3E). This line harbors a constitutive knockin of the GO-ATeam2 construct into the ROSA26 locus under a ubiquitous promoter (CAG), allowing stable and non-conditional expression of the ATP sensor across all tissues and developmental stages. Further validation confirmed that GO-ATeam2 responds within the physiological range of cellular ATP concentrations both *in vitro* and *in vivo*. In permeabilized mouse embryonic fibroblast (MEF) cells, exogenous ATP titration yielded a Hill curve with a K_d of 1.6 mM (Figures S4A and S4B). Additionally, *in vivo* experiments using two-cell-stage embryos from AVID mice—where ATP was decreased by 2-deoxy-D-glucose (2DG) and antimycin A or increased by proAX¹⁸ administration—demonstrated a comparable response curve, with an apparent K_d of 1.36 mM based on parallel luciferase measurements (Figure S5). These results confirm that the sensor accurately detects physiological ATP fluctuations in living tissues.

Multiscale spatial imaging of ATP distribution in the AVID mouse

To evaluate the versatility of the AVID mouse, we first assessed its ability to monitor ATP concentrations at multiple scales, ranging from whole-organism to cellular levels. Using macroscopic imaging, neonatal AVID mouse organs exhibited uniform and physiological GO-ATeam expression, enabling reliable FRET/GFP ratiometric measurements without the need to adjust fluorescence imaging parameters, such as excitation light intensity or exposure time, for each organ. This uniform expression enabled simultaneous and quantitative ATP imaging across thoracic and abdominal organs, including the thymus, heart, lungs, skeletal muscle, liver, pancreas, spleen, kidneys, stomach, intestines, and bladder, within a single field of view (Figure 1A). These results showed a tendency toward higher ATP concentrations in energy-demanding organs such as the heart, skeletal muscle, stomach, and pancreas, which are known to consume substantial energy for contraction-relaxation cycles^{19,20} and digestive enzyme production.²¹ Conversely, ATP concentrations appeared relatively lower in organs such as the liver and small intestine. 22,23 These comparisons were made in male neonatal mice at postnatal day 1, during their natural rest phase (approximately 4:00 p.m.) and after feeding, which was visually confirmed by the presence of milk in the stomach. However, ATP distributions may be influenced by nutritional and developmental states. To validate these findings, we compared our results to previous biochemical measurements. For example, a high-performance liquid chromatography (HPLC)and luciferase-based study²⁴ quantified tissue ATP levels in adult mice and reported relatively low ATP concentrations in the brain and higher concentrations in skeletal muscle, with the heart and liver showing comparable levels. While the heart-liver comparison slightly differs from our findings, the general pattern among the brain, the liver, and skeletal muscle is consistent. Furthermore, magnetic resonance spectroscopy-based measurements²⁵ revealed that ATP concentrations in the heart are higher than in the liver and lower than in skeletal muscle, supporting our observations.

Next, to assess ATP concentration distribution at high resolution at inter- and intracellular levels, we conducted high-resolution two-photon microscopy (2PM) on brain sections where ATP distribution had previously been characterized using conventional mass spectrometry (MS) imaging.²⁶ The AVID mouse successfully detected lower ATP levels in the polymorph layer



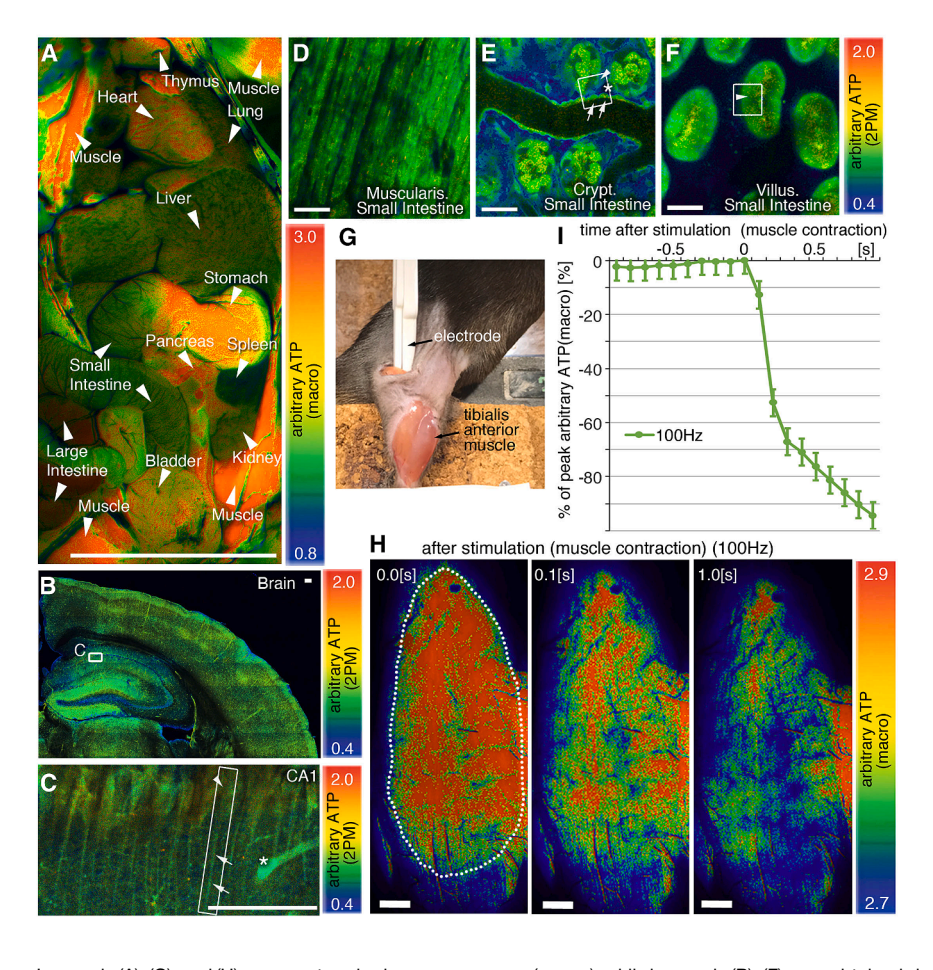


Figure 1. Visualization of ATP concentrations and dynamics in AVID mice

(A) Intravital ATP concentration imaging of thoracic and abdominal organs in a male neonatal AVID mouse (postnatal day 1, n=6) that consumed maternal milk. In AVID mice, GO-ATeam2 is constitutively expressed under a ubiquitous promoter, enabling ATP imaging across all tissues without the need for Cre recombination.

(B) ATP concentration imaging of a brain slice from an adult AVID mouse (n = 8).

(C) Enlarged view of the CA1 region of the hippocampus from (B). White squares highlight pyramidal cells. The arrowhead marks the soma, arrows indicate dendrites of pyramidal neurons, and the asterisk denotes a blood vessel (n = 8).

(D–F) Intravital ATP concentration imaging of the small intestine (n=6), depicting different layers: (D) muscularis, (E) crypt, and (F) villus. In (E), within the white square, the arrowhead marks a Paneth cell, arrows indicate blood vessel cells, and the asterisk represents the lamina propria.

(G) Live mice were immobilized, and electrical stimulation of the sciatic nerve was applied to induce contractions in the tibialis anterior muscle. (H) Intravital ATP concentration imaging of skeletal muscle (n = 6) at 0.0 (left), 0.1 (middle), and 1.0 (right) s after 100 Hz electrical stimulation-induced muscle contraction. The region of interest (ROI) for quantitative analysis is outlined with white dashed lines

(I) Graph illustrating the time-course changes in ATP concentration in skeletal muscle before and after 100 Hz stimulation-induced muscle contraction. Warmer colors represent higher ATP concentrations. Error bars represent mean ± standard deviation (SD).

Images in (A), (G), and (H) were captured using a macroscope (macro), while images in (B)–(F) were obtained via two-photon microscopy (2PM), as indicated on the color bar. Scale bars: 10 mm (A), 100 µm (B–F), and 1 mm (H). The numbers on the color bar correspond to arbitrary ATP concentration values, specifically represented by the FRET/GFP ratio.

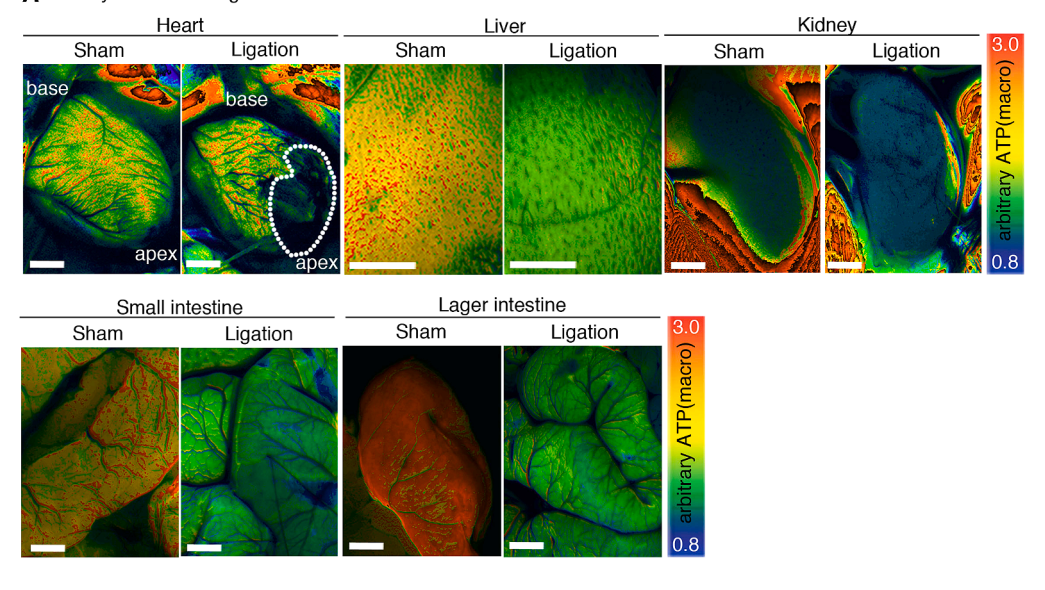
of the dentate gyrus, a region with low mitochondrial density,²⁷ demonstrating high spatial resolution (Figure 1B). Additionally, previously unmeasurable intracellular ATP distributions within neurons were visualized, revealing that the soma (Figure 1C, arrowhead) exhibited higher ATP levels than the dendrites (Figure 1C, arrow). These observations aligned with prior electron microscopy findings on mitochondrial distribution,²⁸ reinforcing the spatial accuracy of ATP imaging in the AVID mouse. To further evaluate ATP concentration monitoring across tissue depths, we used 2PM to observe the intestine from the abdominal side. This approach confirmed ATP measurements at the cellular level across different tissue layers, from the muscular layer in the superficial region (Figure 1D) to the crypts (Figure 1E) and the villi (Figure 1F) in deeper regions. Higher metabolic activity was detected in the muscular layer (Figure 1D), Paneth cells (Figure 1E, arrowhead), vascular endothelial cells (Figure 1E, arrow), and epithelial cells (Figure 1F, arrowhead), while significantly lower ATP concentrations were observed in the lamina propria (Figure 1E, asterisk). These findings highlight the AVID mouse's ability to provide a comprehensive analysis of ATP dynamics across multiple scales, from macroscopic organ-level imaging to microscopic intracellular resolution, establishing it as a powerful tool for studying ATP metabolism *in vivo*.

Millisecond-scale temporal resolution of ATP dynamics in skeletal muscle

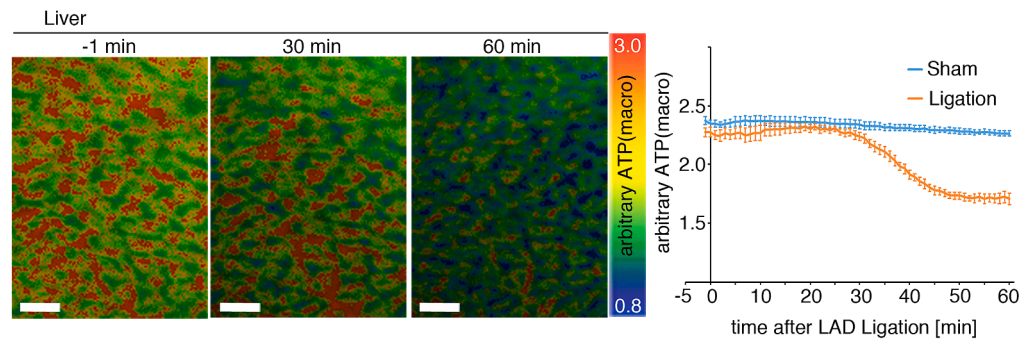
To assess the temporal resolution of the AVID mouse, we analyzed ATP dynamics during skeletal muscle contraction and subsequent recovery, a process characterized by rapid ATP turnover. Conventional magnetic resonance spectroscopy studies have shown that ATP levels decrease by approximately 0.6 mM within 16 s of contraction onset, 29,30 though this measurement is constrained by the limited temporal resolution of the imaging equipment. In this study, we stimulated the tibialis anterior muscle via sciatic nerve stimulation and recorded FRET/GFP ratios at 0.05-s intervals (Figures 1G and 1H; Video S1). Notably, 90% of the ATP depletion observed over 16 s occurred within the first second of contraction, with 50% of depletion already evident within the initial 0.2 s. These findings indicate that ATP consumption is highly concentrated in the early phase of contraction, when tension rapidly increases, while ATP utilization during tension maintenance remains minimal (Figure 1I). This confirms the AVID mouse's capability to monitor



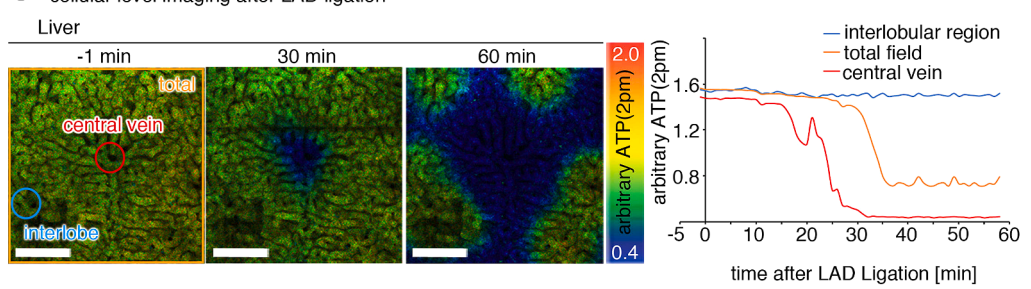
▲ 5 days after LAD Ligation

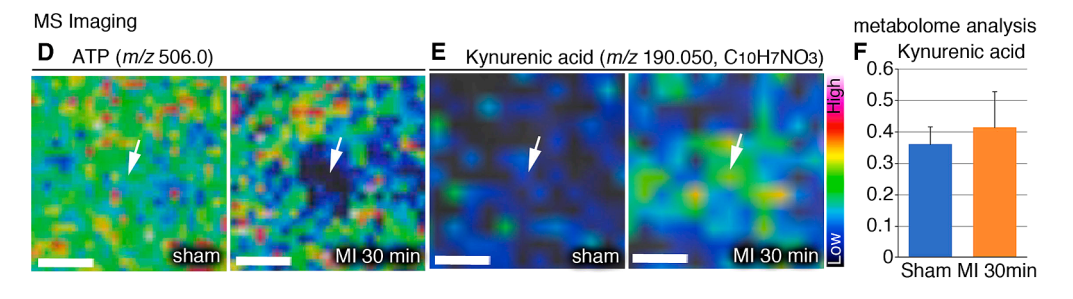


B whole-organism level imaging after LAD ligation



C cellular level imaging after LAD ligation





(legend on next page)

Resource



ATP dynamics at a millisecond temporal resolution. These results indicate that the observed ATP depletion is not confounded by changes in tissue oxygen or pH during the stimulation, as supported by additional physiological measurements (Figures S6 and S7; see limitations of the study).

Furthermore, ATP levels recovered exponentially after stimulation, with a time constant (τ) of 6.85 s (Figure S8), which is consistent with previous phosphocreatine recovery measurements in human skeletal muscle (τ = 5–30 s).³¹ To correlate ATP dynamics with mechanical output, we simultaneously recorded dorsiflexion torque in the same mice. The peak of ATP depletion tightly coincided with the force generation phase, supporting a direct link between contractile activity and ATP consumption (Figure S9).

Systemic and temporal ATP responses following myocardial infarction

To determine whether temporal ATP alterations could be monitored at a whole-body scale, we analyzed multi-organ ATP dynamics following acute myocardial infarction (MI). After inducing MI by ligation of the left anterior descending (LAD) coronary artery in AVID mice, we performed longitudinal imaging of ATP levels in multiple organs over 5 days. Unlike conventional methods that primarily assess cardiac tissue ATP depletion, AVID enabled us to observe a previously unreported systemic metabolic response, with significant ATP reductions in the liver, kidneys, small intestine, and large intestine. Notably, ATP depletion in the intestines occurred within minutes post-infarction, preceding changes in other organs and suggesting an early metabolic signaling event linked to ischemic stress. These findings indicate that MI triggers a rapid, coordinated metabolic response across multiple organ systems, which could not be captured with traditional ATP measurement techniques. (Figure 2A). To corroborate the systemic metabolic decline observed in peripheral organs after MI, we assessed the physiological status of the mice. Echocardiographic analysis confirmed that left ventricular ejection fraction (EF) significantly decreased from 78.2% to 60.9% 5 days post-MI (p = 0.0000031). Concurrently, body weight decreased by an average of 9.8% (SD = 1.1%), in contrast to a 2.0% increase (SD = 0.6%) in sham-operated controls (p = 0.000000027) (Figure S10). These data support the occurrence of sustained cardiac dysfunction and systemic catabolism during the post-MI period. Further high-resolution temporal analysis of ATP levels at minute intervals postligation revealed significant ATP depletion in the small and large intestines as early as 12-13 min after ligation (p < 0.05; Figures S11B and 11C; Videos S2 and S3). Conversely, ATP depletion in the liver and kidneys occurred approximately 20 min later (p < 0.05; Figures 2B and S11A; Videos S4 and S5). These findings suggest that organ network alterations triggered by MI propagate systemically within minutes. The temporal differences in ATP depletion across organs likely stem from variations in blood supply, oxygen demand, and ischemic tolerance, further demonstrating the AVID mouse's ability to precisely capture the spatiotemporal dynamics of disease progression at an organ-network level. To further validate the mechanistic basis of ATP depletion in the liver post-ligation, we assessed hepatic blood flow and tissue oxygenation. We administered Alexa Fluor 647-labeled bovine serum albumin and tracked its distribution in the liver via 2PM, revealing that hepatic blood flow velocity dropped to approximately 60% of the baseline within 10 min after ligation and remained suppressed. In parallel, real-time optical oxygen measurements revealed spatial heterogeneity in hepatic oxygen tension following MI, with some regions exhibiting up to a 48% reduction 60 min after ligation. Although the precise anatomical localization could not be definitively confirmed, the areas with the most significant hypoxia likely correspond to zones typically characterized by lower baseline oxygen levels. These data support the interpretation that hepatic ATP depletion was driven by regional hypoperfusion and hypoxia, further demonstrating the sensitivity and utility of the AVID system (Figures S13 and S14).

Spatially confined hepatic ATP depletion and local metabolic remodeling

In addition to inter-organ ATP dynamics, we further analyzed ATP changes at tissue depth and cellular levels. Using 2PM, we monitored ATP concentration dynamics in the liver, capturing changes at both tissue-depth and cellular resolution. This analysis revealed that ATP depletion did not occur uniformly across

Figure 2. Multi-organ ATP dynamics and spatially confined metabolic remodeling revealed by AVID mouse

(A) Intravital imaging of ATP concentrations in the heart, liver, kidney, small intestine, and large intestine in sham-operated (Sham, n = 8) and left anterior descending (LAD) artery-ligated (Ligation) mice 5 days post-ligation (n = 8).

(B) Intravital ATP concentration imaging of the liver at the whole-organism level during LAD ligation (n = 6). Graph shows time-course changes in ATP concentration in the liver at the whole-organism level during LAD ligation. Red and blue lines represent ATP concentrations in myocardial infarction (MI) mice (n = 6) and sham-operated mice (n = 6), respectively. The vertical axis indicates arbitrary ATP concentrations, while the horizontal axis represents time after LAD ligation (minutes).

(C) Intravital ATP concentration imaging of the liver at the cellular level during LAD ligation (*n* = 6). Red circles mark the central vein, blue circles highlight the large intestinal glands or interlobular region, and yellow squares represent the entire field of view. Graph shows time-course changes in ATP concentration at the cellular level in the liver during LAD ligation. Yellow, blue, and red lines indicate ATP concentrations in the entire field, interlobular region, and central vein, respectively. The vertical axis represents arbitrary ATP concentrations, while the horizontal axis shows time after LAD ligation (minutes).

(D and E) MS imaging of ATP (D) and kynurenic acid (E) distributions in the liver from sham-operated mice (Sham, n = 6) and LAD-ligated mice 30 min after ligation (MI 30 min, n = 6). Arrows indicate the central vein region.

(F) Metabolome analysis of whole liver tissue, comparing kynurenic acid levels between sham-operated mice (n = 8) and LAD-ligated mice 30 min after ligation (n = 8).

Images in (A) and (B) were captured using a macroscope (macro), while images in (C) were obtained using a two-photon microscope (2PM), as indicated on the color bar. Warmer colors denote higher ATP concentrations. Scale bars: 2 mm (A), 1 mm (B), and 100 µm (C–E). The color bar numbers indicate the range of arbitrary ATP concentrations, specifically the FRET/GFP ratio. Error bars represent mean ± SD in (B) and (F).



the liver but rather was spatially restricted to the pericentral region (zone 3)^{32,33} surrounding the central vein (Figure 2C). This localized ATP depletion began approximately 10 min after MI onset and gradually expanded over time, exhibiting a characteristic progression pattern (Figures 2C, blue circles, and 2C, graph, blue line; Video S6). These findings demonstrate that the AVID mouse enables precise monitoring of ATP fluctuations across spatial scales, from the organ level to cellular resolution.

Capitalizing on this high-resolution spatiotemporal ATP mapping, we next aimed to elucidate the metabolic alterations occurring specifically in these spatially confined ATP-depleted regions. To this end, we performed comprehensive metabolome analysis and spatially resolved MS imaging using liver sections obtained 30 min after MI onset, when the ATP depletion pattern was most distinct. Unexpectedly, whole-liver metabolome analysis revealed a significant decrease in lactate concentration, a hallmark of glycolytic activation, rather than the expected increase, along with downward trends in NADH and succinate levels (Figure S11D). These findings suggest that at this early phase (30 min post-MI), the liver as a whole does not experience severe ischemic metabolic stress.

In contrast, MS imaging of the same liver sections identified localized accumulation of kynurenic acid specifically within ATP-depleted areas near the central vein (Figures 2D, 2E, and S12). Importantly, the whole-liver metabolome analysis detected no significant change in kynurenic acid levels (Figure 2F). This observation highlights that the spatially confined metabolic response was only detectable through the combination of AVID-based real-time ATP imaging and high-spatial-resolution MS imaging. This integrated analysis unveiled previously unrecognized local metabolic remodeling, which would have been completely missed by conventional bulk metabolomics.

Furthermore, this early ATP depletion near the central vein raises the intriguing possibility that it serves as a precursor event to subsequent cell death and fibrosis during chronic disease progression.³⁵ Thus, the AVID mouse offers a powerful means to visualize subtle metabolic perturbations occurring at the earliest stages of pathogenesis, enabling the prediction of future disease progression.

DISCUSSION

The AVID mouse represents a transformative resource for spatial systems metabolism research. By providing real-time, multiscale ATP imaging from whole-body to cellular levels, AVID enables seamless integration of macroscopic organ-level imaging with microscopic spatial metabolomics. This combination of high spatial and temporal resolution enables comprehensive visualization of ATP dynamics in living organisms, which will facilitate discoveries in organ-organ communication, metabolic heterogeneity, and early disease signatures, providing a robust platform for future metabolic research and therapeutic development. Furthermore, this spatial systems metabolism framework established by AVID can be further expanded by integrating other spatial omics technologies, such as spatial transcriptomics and proteomics, ultimately paving the way for comprehensive multi-omics spatial systems biology to uncover integrated metabolic regulation in health and disease.

Limitations of the study

Genetically encoded fluorescent biosensors, including GO-ATeam2, can be influenced by environmental factors such as oxygen concentration, pH, and temperature. While the ATP-binding affinity of the sensor's ε subunit and the maturation of fluorescent proteins are known to be sensitive to such conditions, we experimentally assessed two major confounders—oxygen tension and pH—across key tissues during ATP imaging (Figures S6, S7, S13, and S14).

In skeletal muscle, a 10-s stimulation at 100 Hz did not significantly reduce the tissue oxygen concentration or pH, suggesting that the observed ATP depletion reflects true metabolic changes rather than sensor artifacts (Figures S6 and S7). In the liver of mice subjected to MI, local reductions in oxygen tension were detected 60 min after ligation (Figure S13), but the FRET/GFP ratio remained stable under similarly hypoxic conditions (10% O_2 ventilation), indicating the minimal impact of hypoxia on ATP sensor readouts. Likewise, although pH decreased by \sim 0.4 units in the liver after infarction, experimentally induced acidosis via intravenous lactate injection did not significantly affect the FRET/GFP ratio (Figure S14), supporting the robustness of the sensor against mild acidification.

However, users should be aware that the sensitivity of GO-ATeam2 may also be affected under hypothermic conditions. Although not directly tested in this study, lower temperatures could alter the conformational dynamics of the ϵ subunit and the fluorescence properties of the FRET pair, potentially impacting quantitative readouts. Therefore, ATP imaging under hypothermia—such as cold exposure—should be interpreted with caution.

Nonetheless, we acknowledge that more severe or prolonged hypoxic or acidotic conditions may still perturb biosensor behavior. Other environmental factors, such as reactive oxygen species or ionic fluctuations, were not systematically evaluated and could potentially influence fluorescence signals in specific contexts. Therefore, users of the AVID mouse are advised to interpret FRET signals with caution under extreme pathophysiological states or in tissues with markedly altered physicochemical environments.

Finally, although GO-ATeam2 was robustly expressed across all tissues, expression levels varied by organ. Direct fluorescence imaging revealed an up to ~5-fold variation in Kusabira Orange intensity (Figure S15A), which correlated with the ~20-fold differences in protein expression as determined by western blotting normalized to GAPDH (Figure S15B). Immunohistochemistry confirmed broad expression across diverse cell types within each organ, though with some heterogeneity in signal intensity (Figure S15C). While these variations do not substantially affect ATP quantification due to the ratiometric FRET design, users should be aware of potential biases when comparing tissues with markedly different architectures or biosensor expression levels.

In this study, none of the *in vivo* physiological or pathological models presented showed an increase in ATP levels above baseline. Future studies that involve conditions such as acute energy supplementation may help to determine the system's capacity to detect ATP increases.

Resource



RESOURCE AVAILABILITY

Lead contact

Further information and requests for resources and reagents should be directed to and will be fulfilled by the lead contact, Dr. Masamichi Yamamoto (myamamoto@ncvc.go.jp, yamamoto.mailsever@gmail.com).

Materials availability

AVID mice generated in this study are available from Dr. Masamichi Yamamoto upon reasonable request and completion of a materials transfer agreement (MTA). The GO-ATeam2 construct used to generate the AVID mice was originally developed by Dr. Hiromi Imamura (Yamaguchi University) and is available from him under a separate MTA.

Data and code availability

- The metabolomics dataset generated during this study has been deposited in the jPOST repository with the accession number JPST003962 and in ProteomeXchange with the accession number PXD066645.
- The dataset will become publicly available on July 28, 2026. No original code was generated in this study.³⁶
- Data supporting the findings are available from the lead contact upon request.

ACKNOWLEDGMENTS

We thank Mai Samejima and Takashi Musashi for their assistance with cardiac ATP imaging analysis, the members of M. Yanagita's laboratory for assistance with experiments and useful discussions, Yoshitaka Ishihara for electroporation, Eiichiro Uchino for assistance with data analysis, and Janet Rossant and Kazu Kikuchi for helpful discussions and comments. The ROSA26-CAG-STOP-TV vector (no. 408) and Southern probe (no. 395) were gifts from Dr. Tsuneyasu Kaisho and Dr. Katsuaki Hoshino. This work was supported by the JST, PRESTO (JPMJPR14MF to M. Yamamoto); JSPS (KAKENHI grant numbers JP24116703, 24657144, 26670100, 19K22513, 19H03561, and JPMJPF2018 to M. Yamamoto; 19K09527 and 22K09248 to Y.O.; 18KK0442 to H.M.; 16K09491 to N.K.; and 20H03697 to M. Yanagita); AMED (grant numbers JP17gm5010002, 23ama121050j0002, 20ek0610017h 0003, and 21gm1210011h0002 to M. Yamamoto; JP23zf0127003 and 23gm1210009 to Y.S.; and 22gm1210009, 22gm5010002, 22zf01270 03h001, and 22ek0310020h0001 to M. Yanagita); the Naito Foundation; the Mitsui Life Social Welfare Foundation; the Takeda Science Foundation; the Mother and Child Health Foundation; the Uehara Memorial Foundation; the Japan Brain Foundation; the Nakajima Foundation; the Foundation for Dietary Scientific Research; the Lotte Foundation; a Mochida Memorial Foundation for Medical and Pharmaceutical Research grant; the Fukuda Foundation for Medical Technology; the Taiju Life Social Welfare Foundation; the Narishige Neuroscience Research Foundation; the Yasuda Medical Foundation; the Astellas Foundation for Research on Metabolic Disorders; the SENSHIN Medical Research Foundation; the Kowa Life Science Foundation; the Miyata Cardiac Research Promotion Foundation: the Shimadu Science Foundation: the Nakatani Foundation for Advancement of Measuring Technologies in Biomedical Engineering; the Research Foundation for Opto-Science and Technology; Banyu Life Science Foundation International; the Casio Science Promotion Foundation; the Suzuken Memorial Foundation; the Kato Memorial Bioscience Foundation to M. Yamamoto; and the Intramural Research Fund (21-2-7 and 22-B-3 to M. Yamamoto) for the Cardiovascular Diseases of National Cerebral and Cardiovascular Center and Intramural Research Fund (3-1 to H.M.) for Neurological and Psychiatric Disorders provided by the National Center of Neurology and Psychiatry, Japan. This work was partly supported by the World Premier International Research Center Initiative (WPI), MEXT, Japan. This work was also supported by the Platform for Drug Discovery, Informatics, and Structural Life Science from the Ministry of Education, Culture, Sports, Science and Technology, Japan; by the Kyoto University Live Imaging Center; by the NIBB Collaborative Research Program No. 14-602 to M. Yamamoto; and in part by Grant-in-Aid KAKENHI 16H06280 "ABiS."

AUTHOR CONTRIBUTIONS

Conceptualization, M. Yamamoto; funding acquisition, Y.O., H Miwa, N.K., Y. S., M. Yanagita, and M. Yamamoto; investigation, all authors; project administration, M. Yamamoto; supervision, M. Yamamoto; visualization, Y.O., R. O., D.S., S.K., and M. Yamamoto; writing – original draft, N.M., S.K., and M. Yamamoto; writing – review & editing, all authors.

DECLARATION OF INTERESTS

M. Yamamoto is involved in a pending patent related to GO-ATeam mice. H.I. holds a patent for the ATeam probe.

DECLARATION OF GENERATIVE AI AND AI-ASSISTED TECHNOLOGIES IN THE WRITING PROCESS

The authors declare that they did not use generative AI or AI-assisted technologies in the writing or preparation of this manuscript.

STAR*METHODS

Detailed methods are provided in the online version of this paper and include the following:

- KEY RESOURCES TABLE
- EXPERIMENTAL MODEL AND STUDY PARTICIPANT DETAILS
 - Animal models and husbandry
- METHOD DETAILS.
 - O Generation of AVID mice and embryo electroporation
 - Metabolomic and imaging analysis
 - o Cellular validation (MEF system)
 - $\circ\,$ Imaging systems and conditions
 - Quantification of Kusabira Orange fluorescence intensity across organs
 - o Myocardial infarction model
 - Oxygen and pH sensing in tissues
 - o Image Processing and analysis
- QUANTIFICATION AND STATISTICAL ANALYSIS
- ADDITIONAL RESOURCES

SUPPLEMENTAL INFORMATION

Supplemental information can be found online at https://doi.org/10.1016/j.celrep.2025.116246.

Received: March 18, 2025 Revised: July 8, 2025 Accepted: August 13, 2025 Published: September 12, 2025

REFERENCES

- Higgins, C.F., and Linton, K.J. (2004). The ATP switch model for ABC transporters. Nat. Struct. Mol. Biol. 11, 918–926.
- Pollard, T.D., and Borisy, G.G. (2003). Cellular motility driven by assembly and disassembly of actin filaments. Cell 112, 453–465.
- 3. Bessman, S.P., and Geiger, P.J. (1981). Transport of energy in muscle: the phosphorylcreatine shuttle. Science *211*, 448–452.
- Sheng, Z.-H. (2017). The Interplay of Axonal Energy Homeostasis and Mitochondrial Trafficking and Anchoring. Trends Cell Biol. 27, 403–416.
- Berg, J., Hung, Y.P., and Yellen, G. (2009). A genetically encoded fluorescent reporter of ATP:ADP ratio. Nat. Methods 6, 161–166.
- Imamura, H., Nhat, K.P.H., Togawa, H., Saito, K., Iino, R., Kato-Yamada, Y., Nagai, T., and Noji, H. (2009). Visualization of ATP levels inside single living cells with fluorescence resonance energy transfer-based genetically encoded indicators. Proc. Natl. Acad. Sci. USA 106, 15651–15656.



Cell ReportsResource

- Tantama, M., Martínez-François, J.R., Mongeon, R., and Yellen, G. (2013).
 Imaging energy status in live cells with a fluorescent biosensor of the intracellular ATP-to-ADP ratio. Nat. Commun. 4, 2550.
- Arai, S., Kriszt, R., Harada, K., Looi, L.S., Matsuda, S., Wongso, D., Suo, S., Ishiura, S., Tseng, Y.H., Raghunath, M., et al. (2018). RGB-Color Intensiometric Indicators to Visualize Spatiotemporal Dynamics of ATP in Single Cells. Angew. Chem. Int. Ed. Engl. 57, 10873–10878.
- Wu, Z., He, K., Chen, Y., Li, H., Pan, S., Li, B., Liu, T., Xi, F., Deng, F., Wang, H., et al. (2022). A sensitive GRAB sensor for detecting extracellular ATP in vitro and in vivo. Neuron 110, 770–782.e5.
- Hellweg, L., Edenhofer, A., Barck, L., Huppertz, M.C., Frei, M.S., Tarnawski, M., Bergner, A., Koch, B., Johnsson, K., and Hiblot, J. (2023). A general method for the development of multicolor biosensors with large dynamic ranges. Nat. Chem. Biol. 19, 1147–1157.
- Marvin, J.S., Kokotos, A.C., Kumar, M., Pulido, C., Tkachuk, A.N., Yao, J. S., Brown, T.A., and Ryan, T.A. (2024). iATPSnFR2: A high-dynamic-range fluorescent sensor for monitoring intracellular ATP. Proc. Natl. Acad. Sci. USA 121, e2314604121.
- Nakano, M., Imamura, H., Nagai, T., and Noji, H. (2011). Ca²⁺ regulation of mitochondrial ATP synthesis visualized at the single cell level. ACS Chem. Biol. 6, 709–715.
- Trevisiol, A., Saab, A.S., Winkler, U., Marx, G., Imamura, H., Möbius, W., Kusch, K., Nave, K.A., and Hirrlinger, J. (2017). Monitoring ATP dynamics in electrically active white matter tracts. eLife 6, e24241.
- Kioka, H., Kato, H., Fujita, T., Asano, Y., Shintani, Y., Yamazaki, S., Tsukamoto, O., Imamura, H., Kogo, M., Kitakaze, M., et al. (2020). In vivo real-time ATP imaging in zebrafish hearts reveals G0s2 induces ischemic tolerance. FASEB J. 34, 2041–2054.
- Gasterstädt, I., Jack, A., Stahlhut, T., Rennau, L.M., Gonda, S., and Wahle, P. (2020). Genetically Encoded Calcium Indicators Can Impair Dendrite Growth of Cortical Neurons. Front. Cell. Neurosci. 14, 570596.
- Madisen, L., Garner, A.R., Shimaoka, D., Chuong, A.S., Klapoetke, N.C., Li, L., van der Bourg, A., Niino, Y., Egolf, L., Monetti, C., et al. (2015). Transgenic mice for intersectional targeting of neural sensors and effectors with high specificity and performance. Neuron 85, 942–958.
- Direnberger, S., Mues, M., Micale, V., Wotjak, C.T., Dietzel, S., Schubert, M., Scharr, A., Hassan, S., Wahl-Schott, C., Biel, M., et al. (2012). Biocompatibility of a genetically encoded calcium indicator in a transgenic mouse model. Nat. Commun. 3, 1031.
- Anada, T., Kawahara, M., Shimada, T., Kuroda, R., Okamura, H., Setoyama, D., Nagatsugi, F., Kunisaki, Y., Kage-Nakadai, E., Kobayashi, S., and Tanaka, M. (2025). A nucleic acid prodrug that activates mitochondrial respiration, promotes stress resilience, and prolongs lifespan. J. Am. Chem. Soc. 147, 22161–22175. https://doi.org/10.1021/jacs.5c06772.
- Gustafsson, A.B., and Gottlieb, R.A. (2008). Heart mitochondria: gates of life and death. Cardiovasc. Res. 77, 334–343.
- Gan, Z., Fu, T., Kelly, D.P., and Vega, R.B. (2018). Skeletal muscle mitochondrial remodeling in exercise and diseases. Cell Res. 28, 969–980.
- Greiner, J.V., and Glonek, T. (2021). Intracellular ATP Concentration and Implication for Cellular Evolution. Biology 10, 1166.
- Bhargava, P., and Schnellmann, R.G. (2017). Mitochondrial energetics in the kidney. Nat. Rev. Nephrol. 13, 629–646.
- Roberts, R.R., Murphy, J.F., Young, H.M., and Bornstein, J.C. (2007).
 Development of colonic motility in the neonatal mouse-studies using

- spatiotemporal maps. Am. J. Physiol. Gastrointest. Liver Physiol. 292, G930-G938
- Chida, J., Yamane, K., Takei, T., and Kido, H. (2012). An efficient extraction method for quantitation of adenosine triphosphate in mammalian tissues and cells. Anal. Chim. Acta 727, 8–12.
- 25. Gupta, A., Chacko, V.P., and Weiss, R.G. (2009). Abnormal energetics and ATP depletion in pressure-overload mouse hearts: in vivo high-energy phosphate concentration measures by noninvasive magnetic resonance. Am. J. Physiol. Heart Circ. Physiol. 297, H59–H64.
- Morikawa, T., Kajimura, M., Nakamura, T., Hishiki, T., Nakanishi, T., Yukutake, Y., Nagahata, Y., Ishikawa, M., Hattori, K., Takenouchi, T., et al. (2012). Hypoxic regulation of the cerebral microcirculation is mediated by a carbon monoxide-sensitive hydrogen sulfide pathway. Proc. Natl. Acad. Sci. USA 109, 1293–1298.
- Bindokas, V.P., Lee, C.C., Colmers, W.F., and Miller, R.J. (1998). Changes in mitochondrial function resulting from synaptic activity in the rat hippocampal slice. J. Neurosci. 18, 4570–4587.
- Faitg, J., Lacefield, C., Davey, T., White, K., Laws, R., Kosmidis, S., Reeve, A.K., Kandel, E.R., Vincent, A.E., and Picard, M. (2021). 3D neuronal mitochondrial morphology in axons, dendrites, and somata of the aging mouse hippocampus. Cell Rep. 36, 109509.
- Jones, D.A., Turner, D.L., McIntyre, D.B., and Newham, D.J. (2009). Energy turnover in relation to slowing of contractile properties during fatiguing contractions of the human anterior tibialis muscle. J. Physiol. 587, 4329–4338.
- Barclay, C.J. (2015). Energetics of contraction. Compr. Physiol. 5, 961–995.
- Kemp, G.J., Taylor, D.J., and Radda, G.K. (1993). Control of phosphocreatine resynthesis during recovery from exercise in human skeletal muscle. NMR Biomed. 6, 66–72.
- Suematsu, M., Suzuki, H., Ishii, H., Kato, S., Yanagisawa, T., Asako, H., Suzuki, M., and Tsuchiya, M. (1992). Early midzonal oxidative stress preceding cell death in hypoperfused rat liver. Gastroenterology 103, 994–1001.
- Sherlock, S. (1951). The liver in heart failure; relation of anatomical, functional, and circulatory changes. Br. Heart J. 13, 273–293.
- 34. Olenchock, B.A., Moslehi, J., Baik, A.H., Davidson, S.M., Williams, J., Gibson, W.J., Chakraborty, A.A., Pierce, K.A., Miller, C.M., Hanse, E.A., et al. (2016). EGLN1 inhibition and rerouting of α-ketoglutarate suffice for remote ischemic protection. Cell *164*, 884–895.
- Herzer, K., Kneiseler, G., Bechmann, L.P., Post, F., Schlattjan, M., Sowa, J.P., Neumann, T., Marggraf, G., Erbel, R., Gerken, G., et al. (2011). Onset of heart failure determines the hepatic cell death pattern. Ann. Hepatol. 10, 174–179.
- 36. Okuda, S., Yoshizawa, A.C., Kobayashi, D., Takahashi, Y., Watanabe, Y., Moriya, Y., Hatano, A., Takami, T., Matsumoto, M., Araki, N., et al. (2025). jPOST environment accelerates the reuse and reanalysis of public proteome mass spectrometry data. Nucleic Acids Res. 53, D462–D467.
- Benabdellah, F., Touboul, D., Brunelle, A., and Laprévote, O. (2009). In situ primary metabolites localization on a rat brain section by chemical mass spectrometry imaging. Anal. Chem. 81, 5557–5560.
- **38**. Marshall, A.G., and Rodgers, R.P. (2004). Petroleomics: the next grand challenge for chemical analysis. Acc. Chem. Res. 37, 53–59.

Resource



STAR*METHODS

KEY RESOURCES TABLE

| REAGENT or RESOURCE | SOURCE | IDENTIFIER |
|---|--|-----------------------------------|
| Antibodies | SOUTIOL | IDENTIFIER |
| Rabbit anti-Kusabira Orange antibody | MBL | PM051M |
| Mouse anti-GAPDH antibody | Proteintech | 60004-1-lg |
| , | | <u> </u> |
| HRP-conjugated anti-mouse IgG secondary antibody | Proteintech | SA0001-1 |
| HRP-conjugated anti-rabbit IgG secondary antibody | Vector Labs | PI-1000 |
| Chemicals, peptides, and recombinant proteins | | |
| 2-Deoxy-D-glucose (2DG) | FUJIFILM Wako | 046–06483 |
| Antimycin A | Sigma-Aldrich | A8674 |
| proAX | Takahisa Anada (Kyushu University) | MTA required |
| Alexa Fluor 647-labeled BSA | Jackson ImmunoResearch | 009-600-051 |
| Experimental models: Cell lines | | |
| Mouse embryonic fibroblast (MEF) cells | Derived in-house | Not specified |
| Experimental models: Organisms/strains | | |
| AVID mouse | This study | MTA required |
| GO-ATeam2 sensor | Hiromi Imamura (Yamaguchi University) | MTA required |
| Oligonucleotides | | |
| GO-ATeam knock-in allele P1 primer | Eurofins genomics | 5'-AGAGCCTCTGCTAACCATGTTCATGCCTTC |
| GO-ATeam knock-in allele P2 primer | Eurofins genomics | 5'-GTGACACTAAGTCAAACGCGAAA |
| qPCR reactions primer1 (Kusabira Orange) | Eurofins genomics | 5'-AGAGATGACACTACGCGTCACAA |
| qPCR reactions primer2 (Kusabira Orange) | Eurofins genomics | 5'-GTGACACTAAGTCAAACGCGAAA |
| TaqMan probe (Kusabira Orange) | Eurofins genomics | 5'-CCGAGGGCGGCCAATGC |
| Software and algorithms | | |
| ImageJ | NIH | https://imagej.nih.gov/ij/ |
| GraphPad Prism | GraphPad Software | N/A |
| Metamorph | Molecular Device | N/A |
| Other | | |
| Two-photon microscope (Leica TCS SP8 MP) | Leica Microsystems | N/A |
| Leica M165FC Fluorescence Stereo Microscope (macro) | Leica Microsystems | N/A |
| Deposited metabolomics dataset | jPOST/ProteomeXchange | JPST003962/PXD066645 |

EXPERIMENTAL MODEL AND STUDY PARTICIPANT DETAILS

Animal models and husbandry

Animals were housed with up to five animals per cage under a 12-h light/12-h dark cycle, at a constant temperature (20°C–24°C) and humidity (35–55%), with food and water available ad libitum. All animal experiments were conducted following protocols approved by the Committees on Experimental Animal Research of Gunma University, Kyoto University, the National Cerebral and Cardiovascular Center, and Nagoya Institute of Technology. All animal models and procedures adhered to the NIH Guide for the Care and Use of Laboratory Animals.

METHOD DETAILS

Generation of AVID mice and embryo electroporation

The AVID mouse was generated through a systematic screening of promoter and genomic integration strategies to achieve stable and physiological expression of the *GO-ATeam* ATP biosensor across all organs. By integrating *GO-ATeam* into the *ROSA26* locus under the control of a carefully selected ubiquitous promoter, we ensured both consistent expression across generations and





physiological detection of ATP concentrations. This approach overcame the limitations of random transgenesis, such as expression silencing or developmental toxicity, and established AVID as a robust platform for quantitative, multiscale ATP imaging across organ systems *in vivo*. To develop a transgenic mouse model capable of visualizing and analyzing ATP dynamics *in vivo*, we adopted the GO-ATeam sensor. GO-ATeam consists of three components: an orange fluorescent protein (OFP; mKO κ), a variant of green fluorescent protein (GFP; cp173-mEGFP), and the ϵ subunit of FoF1-ATP synthase, positioned between mKO κ and cp173-mEGFP (Figure S1A). Because GO-ATeam can bind ATP and potentially affect intracellular ATP concentrations, it is critical to maintain expression at a level that avoids cellular and systemic toxicity. At the same time, reliable detection of ATP dynamics requires expression levels at least 7-fold higher than tissue autofluorescence (Figure S16). To meet these criteria, we evaluated eight promoters and two gene delivery approaches using embryonic stem (ES) cells (Figure S1B).

In the random insertion approach, GO-ATeam2 expression vectors were constructed under the control of seven representative ubiquitous promoters (β -Actin, CAG, CMV, $EF1\alpha$, MC1, PGK, and UbC), each replacing the CMV promoter region in pcDNA3.1. All vectors included a neomycin resistance cassette driven by the PGK promoter. After linearization, these vectors were transfected into G4 (C57BL/6 \times 129svJ hybrid) ES cells (a kind gift from Dr. Andras Nagy) using FuGENE HD, and transfected clones were selected with G418 (200 μ g/mL). The cells were tested for mycoplasma contamination using a TaKaRa PCR Mycoplasma Detection Set (Takara)and found to be negative.

To quantitatively assess expression levels derived from the ATP probe, *Kusabira Orange* expression was evaluated in the G418-resistant clones. *Kusabira Orange* levels were quantified by TaqMan qPCR, normalized to *GAPDH*, and clones were categorized into high, medium, or low expressers (Figure S2). From each promoter, five clones were randomly selected from each expression group (high, medium, low), yielding 105 total clones for detailed analysis, which were subsequently used for chimera production and *in vivo* imaging validation (Figure S2).

In the knock-in approach, targeting vectors were designed to insert *GO-ATeam2* into the *Rosa26* locus, using two configurations: one employing exogenous promoters and the other using the endogenous *Rosa26* promoter. In the exogenous promoter constructs, each promoter was placed upstream of a floxed transcriptional STOP cassette, thereby overriding transcription from the endogenous *Rosa26* promoter. These vectors were based on modified CTV backbones and included 5' and 3' *Rosa26* homology arms, a *loxP*–STOP–*FRT*–*PGK*–*Neo*–*BGH* polyA–*FRT*–STOP–*loxP* cassette (ROSA26-CAG-STOP-TV vector, a kind gift from Dr. Tsuneyasu Kaisho and Dr. Katsuaki Hoshino), the *GO-ATeam2* sequence, a polyA signal, and a negative selection cassette (*PGK*–*DT-A*–*BGH* polyA).

For the endogenous promoter construct, the pROSA26-1 vector was modified by inserting a *splice acceptor* (SA), followed by a *loxP*–STOP–FRT–PGK–Neo–BGH polyA–FRT–STOP–*loxP*–GO-ATeam2–G-CSF polyA sequence between the homology arms.

All vectors were linearized using Asil and electroporated into G4 hybrid ES cells. Correct targeting was confirmed by Southern blotting using a \sim 700 bp probe located approximately 3 kb upstream of the 5' homology arm of the Rosa26 locus (a kind gift from Dr. Tsuneyasu Kaisho and Dr. Katsuaki Hoshino). The STOP cassette was removed by transient expression of pCre-Pac followed by puromycin selection, and recombination and excision were confirmed by PCR and qPCR. The resulting AVID mice were backcrossed for ten generations to the C57BL/6J background to establish congenic lines.

PCR amplification of the *GO-ATeam* knock-in allele was performed using primers P1 (5'-AGAGCCTCTGCTAACCATGTT CATGCCTTC) and P2 (5'-GTGACACTAAGTCAAACGCGAAA), PCR amplification of the GO-ATeam knock-in allele was performed using primers P1 (5'-AGAGCCTCTGCTAACCATGTTCATGCCTTC) and P2 (5'-GTGACACTAAGTCAAACGCGAAA), resulting in a 342-bp fragment. qPCR reactions used primers 5'-AGAGATGACACTACGCGTCACAA and 5'-GTGACACTAAGTCAAACGCGAAA, along with a TaqMan probe (5'-CCGAGGGCGGCCAATGC) for Kusabira Orange detection, internal control rodent GAPDH (Applied Biosystems).

Ultimately, 121 ES cell clones were aggregated with morula-stage ICR embryos to generate chimeric mice. Male chimeras from each clone were mated with C57BL/6J females to produce F1 heterozygotes and confirm germline transmission. Among the 121 lines screened, only the AVID line exhibited ATP-dependent changes in the FRET/GFP ratio, normal development and fertility, and metabolic traits indistinguishable from wild-type mice. In contrast, many other lines failed to develop, showed no GO-ATeam expression despite successful integration, or exhibited transgene silencing in the F1 or F2 generation—highlighting the limitations of random insertion approaches.

In the AVID knock-in line, however, stable and optimal expression of GO-ATeam was maintained across generations, enabling tissue-wide ATP imaging.

Electroporating single-cell embryos with GO-ATeam2 mRNA: A pair of custom (BEX, Tokyo, Japan) platinum-block electrodes (length, 10 mm; width, 3 mm; height, 0.5 mm; gap, 1 mm) was used. The electrodes, which were connected to a CUY21EDIT II unit (BEX, Tokyo, Japan), were placed under a macroscope. Embryos cultured in mWM medium (ARK Resource, Kumamoto, Japan) were washed three times with Opti-MEM (Thermo Fisher Scientific) to remove the serum-containing medium. The embryos were then placed in a line in the electrode gap filled with RNA-containing Opti-MEM I solution (total 5 μ L), and electroporation was then performed. The electroporation conditions were 30 V (3 ms ON + 97 ms OFF) \times 7 in most experiments. After electroporation, the embryos were immediately collected from the electrode chamber and subjected to four washes with M2 medium (Sigma-Aldrich) followed by two washes with mWM medium. The eggs were then cultured in mWM medium at 37°C in an atmosphere containing

Resource



5% CO₂. The fluorescent signals from the GO-ATeam probe and the autofluorescent signals that coincided with the wavelengths of RFP (for FRET) and GFP markers under the 920nm two-photon excitation light were quantified at 16 bits using a two-photon microscope.

Metabolomic and imaging analysis

Central Metabolic Pathways: Metabolite extraction from tissues for metabolome analyses was performed as previously described. Briefly, liver tissue, along with internal standards (IS), was homogenized in ice-cold methanol (500 μ L) using a manual homogenizer (Finger Masher, AM79330, Sarstedt). Equal volumes of chloroform and 0.4 \times ultrapure water (LC/MS grade, Wako) were added. The suspension was centrifuged at 15,000 \times g for 15 min at 4 $^{\circ}$ C. The aqueous phase was filtered using an ultrafiltration tube (Ultrafree MC-PLHCC, Human Metabolome Technologies) and concentrated using a vacuum concentrator (SpeedVac, Thermo). The concentrated filtrate was dissolved in 50 μ L of ultrapure water and analyzed by LC-MS/MS and IC-MS. To ensure accurate quantification, both internal and external standards were employed. 2-morpholinoethanesulfonic acid (MES) and 1,3,5-benzene-tricarboxylic acid (trimesate) were used as IS for anionic metabolites, while L-methionine sulfone and 3-aminopyrrolidine dihydrochloride were used for cationic metabolites. These IS compounds are not naturally present in tissues, allowing correction for extraction loss by calculating recovery rates. In parallel, authentic external standards for all target metabolites were analyzed in ultrapure water to establish m/z values and retention times for reliable compound identification and quantification.

Spatial Metabolomics by MALDI Imaging: Liver tissues were dissected and embedded in Super Cryoembedding Medium (SCEM)-L1 (SECTION LAB, Hiroshima, Japan), and stored at -80° C until use. The frozen SCEM blocks were sectioned at -16° C using a cryostat (CM 3050; Leica, Wetzlar, Germany) to make liver slices at a thickness of 8 μm and those were thaw mounted onto an indium-tin-oxide (ITO)–coated glass slides (Bruker Daltonics, Billerica, MA, USA). Prepared tissue sections were coated with 2,5-dihydroxybenzoic acid (50 mg/mL dissolved in 80% methanol) or 9-aminoacridine (10 mg/mL, dissolved in 80% ethanol)³⁷ as a matrix for cationic or anionic molecular detection, respectively. Those solutions were manually sprayed with an artistic-brush (Procon Boy FWA Platinum, Mr. Hobby, Tokyo, Japan). MALDI imaging was performed using both Ultraflextreme MALDI-TOF/TOF mass spectrometer (Bruker Daltonics) for anion metabolite imaging, and 7T FT-ICR-MS (Solarix Bruker Daltonik, Bremen, Germany) for cation metabolite, i.e., kyunrenic acid imaging. In the TOF/TOF-MS based imaging analysis, data were acquired in the negative reflectron mode and signals between m/z 50 and 1000 were collected. In the FT-ICR-MS imaging, positive ions between m/z 100 and 300 were collected using the 'continuous accumulation of selected ions' mode. The high mass accuracy provided by FT-ICR-MS allowed for the selective ion signals of the metabolites to be obtained within a mass window of 5 ppm, enabling the identification of the specific elemental composition of the compounds by comparing the highly accurate masses in databases.³⁸ For both analysis, image reconstruction was performed using FlexImaging 4.1 software (Bruker Daltonics).

Energy Expenditure: Metabolic cage analysis was conducted using a feeding and activity monitoring system (MFD-RQ, SHINFACTORY). Animals were habituated to the metabolic cage for three days prior to the experiment. Data collected from days 4–7 was averaged for analysis. Energy metabolism was assessed with an ARCO-2000 magnetic-type mass spectrometric calorimeter (ARCO SYSTEMS). Carbohydrate and fat expenditure, as well as energy expenditure, were calculated using previously described equations. Data was collected every five minutes.

Cellular validation (MEF system)

Cell Lines: Mouse embryonic fibroblasts (MEFs) were derived from 15.5-day-old embryos. Mouse embryos were dissected in PBS, and limbs, internal organs, and the brain were removed. Embryos were washed three times with serum-free DMEM, minced with sterile surgical scissors, and incubated in trypsin/EDTA in PBS at 37°C for 30 min. Cells were pelleted by centrifugation at 200*g* for 5 min, then cultured in DMEM supplemented with 10% FBS. The cells were tested for mycoplasma contamination using a TaKaRa PCR Mycoplasma Detection Set (Takara) and found to be negative.

Permeabilization and Measurement of ATP Concentration in Mouse Embryonic Fibroblasts (MEFs): MEFs derived from knock-in mouse embryos were permeabilized by incubation with 50 mg/mL α -hemolysin (Sigma-Aldrich) in permeabilization buffer (140 mM KCl, 6 mM NaCl, 0.1 mM EGTA, 10 mM HEPES, pH 7.4) for 30 min in a CO $_2$ incubator. The permeabilization buffer was replaced with calibration buffer (140 mM KCl, 6 mM NaCl, 0.5 mM MgCl $_2$, 10 mM HEPES, pH 7.4) containing varying Mg-ATP concentrations (0–20 mM). Permeabilized MEFs were observed with an inverted multiphoton microscope.

Imaging systems and conditions Imaging conditions

The imaging system consisted of a TCS SP8 MP multiphoton microscope (Leica), driven by a Mai Tai HP Ti laser (Spectra-Physics) tuned to 920 nm for GFP excitation, and an inverted microscope equipped with an HC FLUOTARL 25×/NA0.95 water-immersion objective (Leica). Cells expressing GO-ATeam were detected using a bandpass emission filter set to 525/50 nm for EGFP and 585/40 nm for Kusabira Orange with a DM560 dichroic mirror. The macroscopic imaging system included an M165FC fluorescence macroscope equipped with a PLAN APO 1.0× objective lens (Leica). Organs were exposed to excitation light (ET470/40), and images were captured using a dual-view fluorescence cMOS camera (ORCA-Flash 4.0, Hamamatsu Photonics, Japan). Fluorescence emissions were resolved using D515/30, DM540, and D575/40 filters.





Early embryo imaging

For two-cell stage embryos, embryos were collected from plugged females and placed in pre-warmed KSOM medium (37°C) on a glass-bottom dish. Fluorescence images were acquired using a multiphoton microscope (TCS SP8 MP, Leica) under constant temperature and humidity, and FRET/GFP ratio images were calculated after background subtraction.

Intravital imaging of organs

Mice were anesthetized with 1.5%–2.0% isoflurane, intubated, ventilated, and continuously monitored with an ECG. Hair was shaved with an electric clipper. The thoracic and abdominal cavities were opened using an electric cautery, and the mouse was positioned in a custom restraint with body temperature maintained using a stage heater (Tokai Hit). Analgesics, including meloxicam (Metacam) or buprenorphine, were administered as needed. Organs were imaged using either an inverted multiphoton microscope (TCS SP8 MP, Leica) with an HC FLUOTARL $25 \times /NA0.95$ water objective, or a fluorescence macroscope (M165FC, Leica) with a PLAN APO 1.0×0 0 objective. For liver imaging following lactate administration, $200 \mu L$ of 1 M lactic acid per 30 g body weight was injected into the inferior vena cava over 30 s, and the liver was imaged under a fluorescence macroscope (M165FC and TCS SP8 MP, Leica. Time-series changes in FRET/GFP ratio were monitored to evaluate ATP fluctuations in liver tissue *in vivo*.

Organ slices

Mice were anesthetized with 4.0% isoflurane. Brains were immersed in cooled Ringer's solution and bubbled with 95% O_2 and 5% CO_2 using Ibuki #180 air stones (Ibuki, Japan). Brain slices (300- μ m thickness) were prepared using a vibratome slicer (VT 1000S, Leica), immediately placed in a chamber supplied with Ringer's solution, and positioned on the microscope stage. Each slice was imaged using an inverted multiphoton microscope.

Imaging of muscle contraction

Mice were anesthetized with 1.5%–2.0% isoflurane, the leg hair was shaved, and the skin was removed from the leg. To detect fluorescence, the leg was immobilized in a custom restraint and kept warm with a stage heater (Tokai Hit). The exposed tibialis anterior (TA) muscle was observed with a fluorescence macroscope. Muscle contractions were induced by electrical stimulation of the sciatic nerve (100 Hz, SEN-3401, SS-203J-DT, Nihon Kohden). To monitor ATP dynamics during and after contraction, macroscopic FRET imaging was performed. Real-time fluorescence signals were recorded before, during, and after stimulation, and the FRET/GFP ratio was calculated to assess ATP depletion and recovery kinetics within the TA muscle.

Western blotting and protein expression analysis

Major organs were collected from three neonatal AVID mice and homogenized in TNE lysis buffer. Homogenates were centrifuged at $12,000 \times g$ for 10 min at 4° C, and the supernatants were collected. Equal amounts of total protein ($20 \mu g$ per lane) were loaded onto 10%–20% gradient SDS-PAGE gels (ATTO) and transferred to PVDF membranes. Membranes were blocked with 5% skim milk and incubated with a rabbit anti-Kusabira Orange antibody (MBL, PM051M; 1:2,000 for Western blotting) and a mouse anti-GAPDH antibody (Proteintech, Cat#60004-1-Ig; 1:50,000). HRP-conjugated secondary antibodies were used for detection: anti-rabbit IgG (Vector Labs, Cat#PI-1000; 1:5,000) and anti-mouse IgG (Proteintech, Cat#SA0001-1; 1:50,000). Chemiluminescent signals were visualized by ECL, and densitometric analysis was performed to quantify GO-ATeam2 expression relative to GAPDH.

Immunohistochemistry

Paraffin-embedded tissue sections were deparaffinized, rehydrated, and subjected to antigen retrieval. After blocking, sections were incubated with a rabbit anti-Kusabira Orange antibody (MBL, PM051M; 1:500 for immunostaining), followed by an HRP-conjugated anti-rabbit IgG secondary antibody (Vector Labs, Cat#PI-1000; 1:5,000). Immunoreactivity was visualized using DAB chromogen. The stained sections were dehydrated, mounted, and observed using a bright-field microscope to assess the tissue distribution of GO-ATeam2.

Quantification of Kusabira Orange fluorescence intensity across organs

To estimate GO-ATeam2 protein expression in each organ, tissues from AVID neonates were imaged using a Leica M165FC fluorescence macroscope equipped with a dsRed filter set (excitation: 540–560 nm; emission: 590–620 nm). Kusabira Orange was excited directly, and the resulting emission intensity was measured. Fluorescence images were captured under standardized exposure conditions, and the mean fluorescence intensity in each organ was quantified. Autofluorescence signals from corresponding wild-type tissues were also measured using the same settings and subtracted from AVID signals to obtain corrected Kusabira Orange intensity values.

Myocardial infarction model

Mice were anesthetized with 1.5%–2.0% isoflurane, intubated, and ventilated. The left anterior descending artery was accessed by lateral thoracotomy and pericardiectomy. Ligation of the left anterior descending artery was performed using an 8-0 suture placed caudal to the left atrial appendage. Ligation was confirmed by myocardial blanching and electrocardiogram (ECG). The wound was closed in layers with a 6-0 suture and Aron Alpha A. Postoperative monitoring was performed, and meloxicam (Metacam) or buprenorphine was administered as needed for analgesia. As outcome indicators of myocardial infarction, body weight, and cardiac ejection fraction (EF) were assessed.

Resource



Oxygen and pH sensing in tissues

Measurement of oxygen partial pressure (pO_2): Tissue oxygenation was measured using an optical oxygen monitor (FireSting O_2 , PyroScience) with a needle-type sensor (OXR50-HS). Calibration was performed using water saturated with room air and water bubbled with 100% nitrogen, following the manufacturer's two-point calibration protocol. Under a dissection microscope, the sensor was manually inserted approximately 1 mm into the tissue using a manual micromanipulator (Leica Microsystems). For skeletal muscle, the tibialis anterior (TA) was exposed and measured; for liver, the probe was inserted into the parenchyma. Measurements were obtained within 5 min after insertion. After each measurement, the sensor tip was rinsed with water to remove any blood, and its functionality was verified using air-saturated water.

Measurement of pH in tissues: Tissue pH was measured using a micro pH electrode (6252-10D, Horiba, Japan) and a portable pH meter (D-51S, Horiba). For pH perturbation experiments, $200 \, \mu L$ of 1 M lactic acid per 30 g body weight was injected into the inferior vena cava over 30 s under isoflurane anesthesia. pH was recorded every second.

Image Processing and analysis

Image Processing: Images of Kusabira Orange and EGFP fluorescence were analyzed with MetaMorph software (Molecular Devices). ImageJ was used for movie editing and linear intensity adjustment solely for visualization purposes. The StackReg plugin in ImageJ was employed to eliminate XY drift in time-lapse series. Fluorescence intensities of EGFP and Kusabira Orange were quantified at 16-bit resolution using MetaMorph and ImageJ. Location data for each brain region was obtained from the Allen Reference Atlas - Mouse Brain coronal sections (http://atlas.brain-map.org/). For non-brain organs, ratio values were calculated by manually selecting ROIs in MetaMorph and extracting intensity values, which were subsequently analyzed in Excel. For quantification of ATP and KYNA distribution from MS imaging, grayscale images (8-bit, 0-255) were generated from the original ion images. Regions of interest (ROIs) were defined as a 100 µm diameter circle centered at the arrow tip in Figures 2D and 2E ("central vein"), and the rest as "other." Pixel intensity histograms were calculated for each ROI using ImageJ.

QUANTIFICATION AND STATISTICAL ANALYSIS

Data are expressed as the mean \pm SD. Statistical analysis was performed using unpaired two-tailed Student's t-test for comparison of two groups and analysis of variance (ANOVA) where appropriate ($^*p < 0.05$; $^**p < 0.01$; NS, not significant). All data were normally distributed, and variances were similar across groups. Biological replicates were conducted using samples from different animals. Results represent data from at least three independent experiments. Sample sizes were estimated based on observed variations and means, with the fewest animals required for statistically valid conclusions. Mice exhibiting abnormal size, weight, or symptoms of disease prior to experiments were excluded as per protocol; however, all mice used were phenotypically normal and healthy. For ratio imaging analyses, Hill fitting and exponential fitting of FRET/GFP ratio changes were performed using GraphPad Prism to quantify ATP responses and recovery kinetics.

ADDITIONAL RESOURCES

Data supporting the findings of this study are available from the corresponding authors upon reasonable request.